LEAVE THIS PAGE BLANK

DO NOT DELETE THIS PAGE

From Tile to Filament

A Cohesive Lamination Method for Scaffold-Free 3D Concrete Printed Vaults

Abdallah Kamhawi
Taubman College of Architecture and Urban Planning, University of Michigan.

Mania Aghaei Meibodi
Taubman College of Architecture and Urban Planning, University of Michigan.

Jesse Capecelatro
Department of Aerospace and Department of Mechanical Engineering, Engineering, University of Michigan.

1 The completed barrel-vault demonstrator (span 1200 mm, rise 300 mm), printed scaffold-free with the cohesive lamination method developed here.

ABSTRACT

Robotic 3D concrete printing can eliminate bespoke formwork for vault construction, but scaffold-free printing remains largely restricted to shells that are self-stable at every stage of fabrication. In the process studied here, primary filaments are deposited side by side along the vault surface, causing the active front to cantilever progressively beyond the region that has already stabilized. We introduce a cohesive lamination method in which a secondary zig-zag filament is deposited over this active front and tied back to earlier material, creating discrete tension ties that prevent peel failure. Inspired by Guastavino's cohesive tile vaulting, the method is developed in two coupled parts. A Discontinuous Galerkin finite element model with mixed-mode cohesive interlayer interfaces resolves delamination and identifies the governing failure location and onset in a primary-only deposition sequence. A reduced-order framework then screens candidate zig-zag patterns, defined by restraint-node count and tie-back depth, using two closed-form checks: deposition survivability before the zig-zag bonds and cycle-to-cycle sustainability after engagement. The framework returns an admissible domain rather than a single solution. In a full-scale barrel-vault demonstrator, the primary-only sequence failed by peel at the root interface after three unsupported filaments, whereas a selected admissible lamination completed the vault without internal scaffolding. The results demonstrate that construction-stage interfacial mechanics can be used as a design lever to extend scaffold-free 3DCP to vaults that pass through cantilevering states.

2

2 A speculative vision of the future of construction. Just as traditional brick vaults are assembled on site without scaffolding, guided only by lightweight timber centering, as shown on the left in Guastavino's method, concrete could one day be deposited in layers directly onto curved surfaces by multiple climbing robots, eliminating the need for formwork or scaffolding (right).

INTRODUCTION

Vaults are among architecture's oldest and most structurally efficient forms. By distributing loads purely through compression, they form long-span slabs that are difficult to realize with conventional bending systems, and they do so with minimal material (Block 2009; Heyman 1966; Ochsendorf 2010). Vaults shaped the spatial vocabulary of Roman, Gothic, and Mediterranean architecture, and they returned in the early twentieth century in the thin-tile work of Rafael Guastavino, whose firm built more than a thousand vaulted ceilings across the United States without internal scaffolding (Guastavino 1893; Ochsendorf 2010). Despite this lineage, vaults have been largely absent from contemporary construction. Two factors account for the decline: the shortage of craft labor with the tacit knowledge required for vault construction, and the need for bespoke internal scaffolding and formwork, which generates substantial waste and cost (Meyer and Sheer 2005; Tang 2015; Scheder-Bieschin, Van Mele, and Block 2024).

Robotic 3D concrete printing offers a path to reviving vault construction. The technology delivers continuous, automated deposition along curved paths and removes the need for bespoke formwork (Buswell et al. 2018; Mechtcherine et al. 2020). This paper extends current research on 3DCP vaults by enabling scaffold-free 3DCP of vaults whose construction passes through substantial cantilevering states.

In 3DCP, vaults' geometric freedom is constrained by the rheology of the fresh material. Unlike thermoplastic or metal additive processes, which solidify upon deposition through rapid thermal phase changes, 3DCP depends on hydration chemistry and thixotropic structuration: the extruded paste remains in a highly deformable green state for seconds to minutes after exiting the nozzle (Roussel 2018; Wangler et al. 2016). When a fresh filament is deposited without underlying support, it acts as a soft cantilever under its own weight, lacking the flexural and shear rigidity to resist gravity, and it sags and peels away from the material behind it (Suiker 2018; Wolfs, Bos, and Salet 2018).

To address this challenge, this paper develops a cohesive lamination method. Primary filaments are deposited side by side along the vault surface, so the active front progressively cantilevers beyond the region that has already stabilized. After each primary deposition increment, a secondary zig-zag filament is deposited over the active front and tied back to earlier material, creating diagonal tension branches that restrain peel at the root of the cantilever. The method therefore reframes scaffold-free vault 3DCP as a problem of controlling interfacial mechanics during construction. Its conceptual precedent is Guastavino's system of cohesive construction: thin tiles laid in multiple overlapping courses and bonded with fast-setting mortar, so that each new course cross-bonded the joints of the one below. In this context, cohesive refers to the mechanical continuity created by bonded layers whose interfaces can transmit stresses across the structure. This interfacial cohesion gave Guastavino vaults their capacity to cantilever during incomplete construction states. The method developed here translates that principle into a robotic 3DCP process.

The contribution is developed and validated in three steps: (a) a finite element model diagnoses the governing failure mode and its localization in a primary-only deposition schedule; (b) a reduced-order design framework uses that localization to screen zig-zag laminations defined by restraint-node count and tie-back depth; and (c) the selected design is validated on a full-scale barrel-vault demonstrator (Figure 1). The method establishes a basis for future multi-robot scaffold-free vault printing (Figure 2).

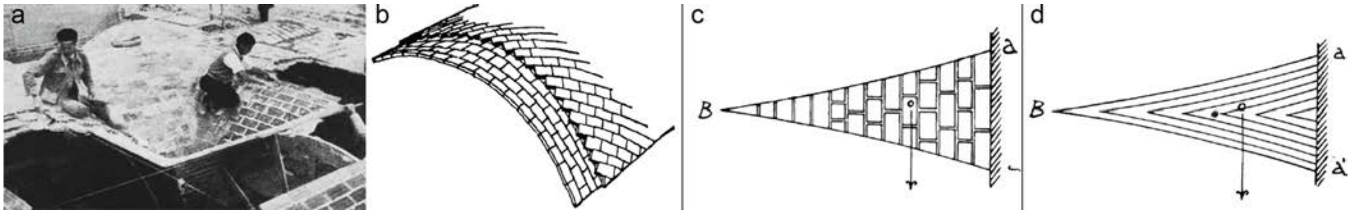

3

4

STATE OF THE ART

Guastavino's tile vaulting provides the conceptual precedent (Figure 3). Masons laid thin tiles at the growing vault edge using fast-setting mortar, then placed subsequent courses diagonally to break joints and make the shell act cohesively (Guastavino 1893; Collins 1968; Ochsendorf 2010). The contribution was not the vault form alone, but cross-bonded lamination, which redistributed local demand through interlocking joints and allowed incomplete shells to cantilever. Here, the cross-bonded course becomes a secondary deposited filament, the mortar becomes a wet-on-wet bond, and the tile becomes a continuous robotic path. The retained principle is a compression-aligned primary layer tied back by a diagonally bonded secondary layer.

Contemporary 3DCP vault research follows two main directions (Figure 4). Assembly approaches print discrete voussoirs, blocks, panels, or ribs in stable orientations and assemble them on temporary supports (Borg Costanzi et al. 2018; Bhooshan et al. 2022; Dell'Endice et al. 2023; Brodmann et al. 2024). Continuous-deposition approaches avoid scaffolding by restricting geometries to forms that remain self-stable throughout printing (Carneau et al. 2019, 2020; Motamedi et al. 2022; Jipa et al. 2024). The present method extends scaffold-free deposition to vaults whose construction includes substantial cantilevering states.

METHODS

Consider a scaffold-free 3DCP vault whose partially built shell must remain stable as the print head advances. **Primary filaments** are deposited side by side along the shell surface, follow the local thrust line, and bond to the previous filament through a wet-on-wet **interlayer interface**. After the frame-supported startup zone—the initial set of primary filaments carried directly by the steel support—each new filament is supported only through its wet-on-wet bond to the preceding filament. The cantilever therefore grows from the last stabilized region, and the self-weight moment at the **root interface**, the boundary between stable and unsupported material, increases with unsupported depth. When that moment exceeds the still-maturing interface capacity, the cantilever peels away and the print fails (Figure 5).

Throughout this paper, **supported** refers only to material carried directly by the external frame; **stabilized** refers to previously printed material whose developed bonds can receive load from the lamination; **unsupported** refers to the active cantilever beyond the current root interface and without external geometric support; and **maturing** refers only to the time-dependent evolution of material or bond properties.

To prevent this peel failure at the root interface, we introduce a zig-zag lamination: a ary filament deposited on top of the primary layer in a path that alternates diagonally between the most recently printed (still unsupported) primary filament and an earlier filament lying within the stabilized region. Each diagonal branch acts as a tension tie that redirects part of the cantilever's self-weight back into the bonded material behind the root interface.

A zig-zag pattern is defined by two discrete design parameters (Figure 6):

1. **Restraint-node count:** how many tie-back points are distributed along the active filament.

2. **Tie-back depth:** how far back into the stabilized region each diagonal branch reaches, measured in primary-filament spacings.

These two parameters fully describe a candidate lamination. The design problem we solve in later sections is to select values of these two parameters that keep the partially built vault stable at every moment of fabrication.

The printing sequence proceeds in alternating cycles (Figure 7). First, one or more primary filaments are deposited along the vault thrust line. A zig-zag pass is then deposited over the active front. In the experiments, no intentional dwell time was introduced between the primary and zig-zag passes. For the reduced-order framework, each cycle is represented by

5

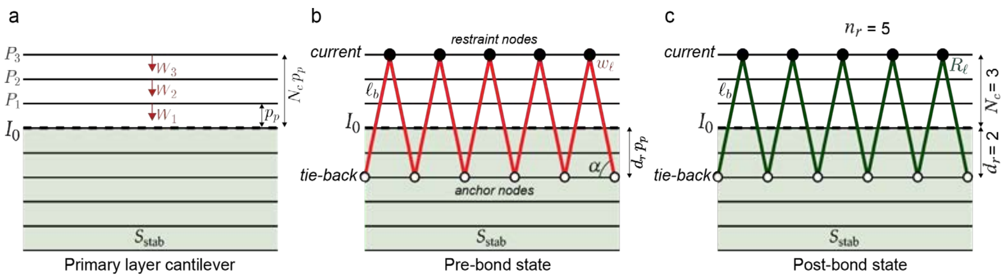

6

3 Guastavino's cohesive tile vaulting: workers at the growing edge (a), axonometric of laminated courses (b), and plan views of the cross-bonded first and second courses (c, d).

4 Existing 3DCP approaches: prefabricated elements assembled on temporary scaffolding (a, b) and directly printed self-stable shells (c).

5 Peel failure at the root interface in a primary-only 3DCP vault print. The cantilevering filaments delaminate from the previously stabilized material once the self-weight moment exceeds the still-maturing capacity of the wet-on-wet interlayer bond.

6 Geometric reference for the primary-layer cantilever (a), pre-bond state (b), and post-bond state (c). S_{stab} denotes the stabilized region and I_0 the current root interface; remaining symbols are defined in the text.

two limiting states. During zig-zag deposition, the complete secondary filament is treated as an unbonded dead load, and Check 1 is evaluated at the end of the pass. After the pass, the diagonal branches are treated as structurally engaged for Check 2. Continuous wet-on-wet bond development during the pass is not resolved explicitly; its effect is represented through the time-dependent root-interface capacity and the capacity-impairment factor β, defined as the fraction of zig-zag deposition time credited toward capacity growth while the root interface is already loaded. The same zig-zag geometry can therefore be stabilizing or destabilizing depending on whether its post-bond restoring action compensates for its pre-bond weight.

We develop the presented method in two coupled parts. First, we develop a finite element model (FEM) of the partially printed vault, used to identify the dominant failure mode as filaments are progressively added. We need this model, rather than reusing an existing 3DCP buildability FEM, because existing models cannot represent the interlayer delamination mode that governs cantilever failure here. Second, we develop a reduced-order design framework that takes the FEM's main result—that failure concentrates at a single governing interface—and turns it into a closed-form design tool that generates admissible lamination parameters.

The Finite Element Model: Resolving Interlayer Delamination

The FEM is diagnostic: it identifies the governing failure mode, the interface at which damage localizes, and the unsupported depth at failure onset. It does not model candidate zig-zag geometries or directly select restraint-node count or tie-back depth. Once failure is shown to localize at one root interface, the reduced-order framework evaluates candidate laminations through interface-level checks rather than a full nonlinear simulation for every pattern.

Why a new FEM is needed. Current 3DCP buildability FEMs treat the printed structure as a continuously bonded medium using a continuous Galerkin formulation, that is, all the deposited material is treated as a single block of concrete with no allowed delamination (i.e., displacement jumps) between filaments of different layers, and they predict buildability failure only in the bulk of the filament (i.e., concrete yielding or buckling) (Suiker 2018; Wolfs, Bos, and Salet 2018; Mechtcherine et al. 2020). Because these models do not allow displacement jumps between layers, they cannot represent the failure mode that actually governs our cantilever: not yielding or buckling within the filament, but the layers peeling apart at their interface (delamination). What is needed is a method that allows the layers to come apart at the interface (a discretization that admits displacement jumps at interlayer interfaces), so delamination is resolved directly.

Our FEM formulation. We model each deposited filament as a discrete object made up of multiple finite elements, with its own independent degrees of freedom (Figure 8). This is a Discontinuous Galerkin formulation: adjacent filaments are not glued at the mesh level. Instead, the boundary between two filaments is governed by an interface law that controls how much they can slip and separate before they delaminate (lose their bond and pull apart). This formulation lets the failure mode emerge from the simulation rather than be assumed in advance: bulk yielding inside a filament and interfacial peeling between filaments are both possible. The benefit for our problem is that we can directly identify which interface fails and when, which is exactly the information the design framework needs.

Interior facets of the mesh are of two kinds (Figure 9): (a) intra-layer facets: boundaries between elements that belong to the same deposited layer,

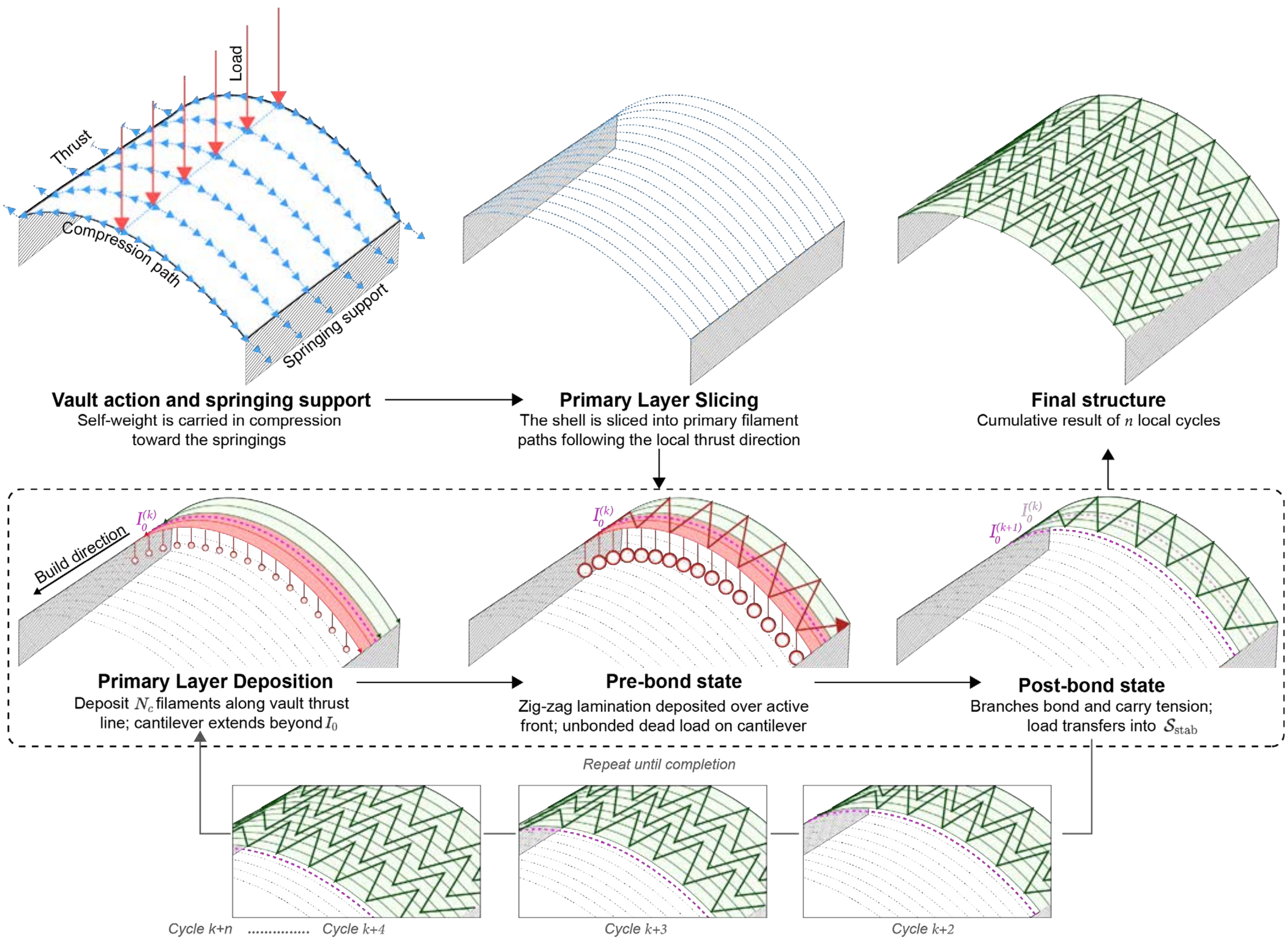

7

which behave as a bonded continuum and are coupled by a symmetric interior penalty; and (b) interlayer facets: boundaries between elements that belong to consecutively deposited filaments, which correspond to physical interlayer boundaries and are governed by a mixed-mode cohesive traction-separation law. The strength and fracture energy of this law depend on the rheological state of the substrate at the moment the new filament is deposited, so that a short rest time yields a strong bond through mechanical intermixing, while a long rest time produces a weak cold joint (Keita et al. 2019; Sanjayan et al. 2018).

Inside each filament, the material is modeled with a rate-dependent viscoplastic law (specifically, a von Mises yield surface with Perzyna viscoplastic regularization). The mechanical properties of the filament evolve with concrete age through a small set of rheological inputs derived from Roussel's thixotropy model for fresh concrete (Roussel 2006): a freshly extruded filament is soft and weak, and stiffens over time.

Filament cells are progressively activated as the print head deposits them, through a smooth birth function that ramps each filament's contribution from inactive to fully deposited over a narrow time interval. The single unified formulation handles both bulk yielding inside filaments and separation between filaments, and the dominant failure mode is not specified in advance but emerges from the equilibrium solve.

The Reduced-Order Design Framework: From Simulation Result to a Design Screening Tool

In the primary-only case (Section 4.2), the FEM localizes damage at the root interface between stabilized and unsupported material; no other interface develops damage. This localization enables a reduced-order screening framework that operates at that interface. Given material properties, vault geometry, and process settings, it returns admissible zig-zag patterns parameterized by restraint-node count and tie-back depth (Figure 10).

For a cantilever of N primary filaments, the screening uses the primary self-weight moment, the unbonded zig-zag dead load, and the restoring force after engagement. The primary moment is $\mathrm{Mp} = ½\, W_p\, p_p\, N^2$ (Eq. 1), where M_p is the root moment, Wp the weight of one primary filament, p_p the center-to-center spacing, and N the unsupported-filament count. Once bonded, each diagonal branch is limited by filament rupture or interfacial shear: $T_b = \min(A_\ell\, \sigma_\ell^{cap}, \tau_{\ell p}^{cap}\, b_\ell\, \ell_b)$ (Eq. 2), where T_b is branch capacity, A_ℓ and b_ℓ are lamination area and effective bonded width, σ_ℓ^{cap} and $\tau_{\ell p}^{cap}$ are admissible axial and bond-shear stresses, and ℓ_b is bonded branch length. The two limits are equal at $\ell_b^* = A_\ell\, \sigma_\ell^{cap} / (\tau_{\ell p}^{cap}\, b_\ell)$.

For $\ell_b < \ell_b^*$, capacity is bond-shear governed; beyond ℓ_b^*, added length

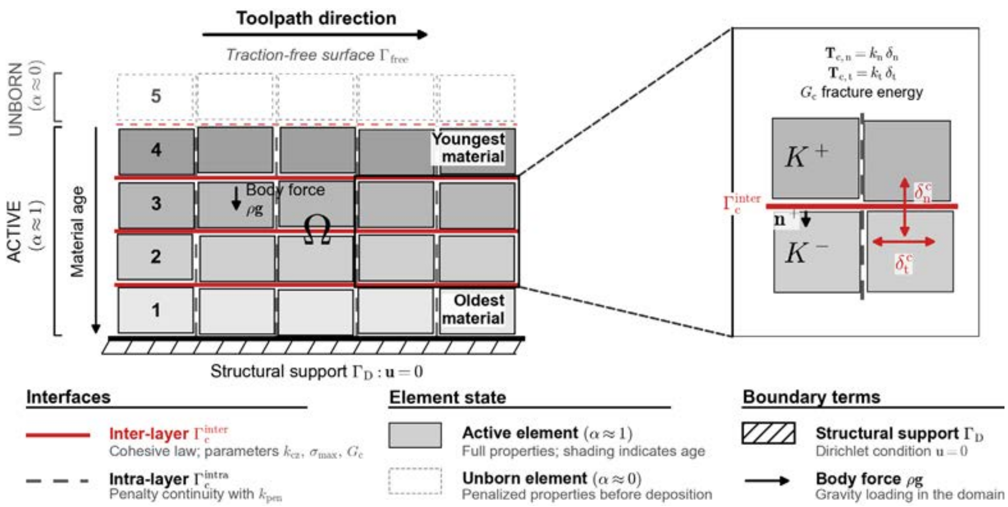

8

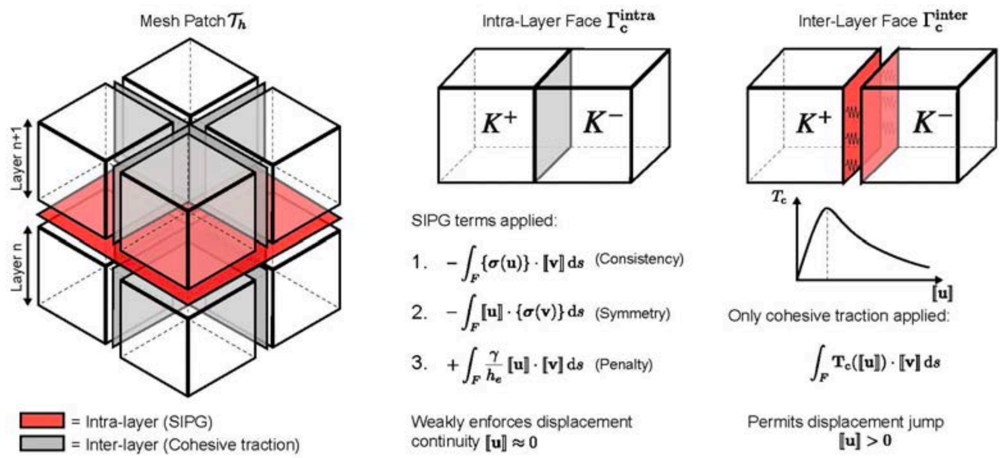

9

7 Local cycle-by-cycle propagation of the zig-zag lamination. Each cycle proceeds in three states: primary filaments cantilever beyond the current root interface, a zig-zag is deposited over the active front as unbonded dead load, then the branches bond and the root interface advances. Bright red and green mark the active cycle; faded green marks previously stabilized cycles.

8 Problem domain. The printed structure (Ω) is built up layer by layer along the toolpath direction. Material ages with time since deposition, so lower layers are older than upper layers. Elements scheduled for later deposition are unborn: their stiffness and weight are suppressed until their deposition time. Gravity acts only within the active material. Element interfaces are shown for context and detailed in Figure 9.

9 Dual interface treatment of the FEM: intra-layer faces coupled by symmetric interior penalty terms (left); interlayer faces governed by a cohesive traction (right).

increases dead load but not capacity (Figure 11). At fixed tie-back depth d_r, increasing restraint-node count n_r adds branches and post-bond restoring action, but also reversals, turn deposits, path length, and pre-bond weight. At fixed n_r, increasing d_r reaches older anchorage and increases branch length and lever arm, but adds weight to every branch. The engagement fraction η scales nominal branch action to account for incomplete contact, age gradients, and substrate compliance.

Candidates are evaluated at two cycle states. In the pre-bond state, the root interface must carry the primary cantilever and complete unbonded zig-zag at the end of deposition: $M_p + \Delta M_\ell^{load} \leq M_I^{cap}$ (Check 1). In the post-bond state, engaged branches must provide at least the primary weight added during that cycle: $n_r(R_\ell - 2\mu_\ell \, \ell_b) \geq W_p \, N_c$ (Check 2). Here, ΔM_ℓ^{load} is the unbonded zig-zag moment, M_I^{cap} the root capacity at pass completion, R_ℓ the effective restoring force per restraint node, μ_ℓ the lamination weight per unit length, and N_c the primary filaments per cycle. A design is admissible only if both checks pass. Check 1 sets an upper boundary as branches and tie-back depth increase pre-bond demand; Check 2 sets a lower boundary where branch action is insufficient. The result is a family of admissible designs.

VALIDATION: A BARREL-VAULT DEMONSTRATOR

Validation used a full-scale barrel vault and followed five steps: describe the setup, print and simulate a primary-only case, calibrate empirical inputs, construct the admissible domain, and print the selected design.

Geometry, fabrication setup, and material system

The demonstrator is a barrel vault with a span of 1200 mm and a rise of 300 mm. The vault cross-section is a circular arc of radius 750 mm, and each primary filament traces an arc of length approximately 1391 mm. Adjacent primary filaments are spaced 14 mm center-to-center. The vault was printed on a custom steel support frame that provides the springing/startup zone condition (Figure 12). The frame-supported startup zone contained ten primary filaments, corresponding to a supported depth of 140 mm; the initial root interface is the first interlayer boundary outside this zone. No internal centering, falsework, or formwork was placed beneath the cantilevering region beyond the startup zone.

The fabrication platform comprises a six-axis industrial robot mounted on a linear rail as the seventh axis, an inline two-component mixing head at the end effector, a screw pump operating at 1.4 L/min, and an accelerator dosing unit. The base material is a commercial 3D-printing mortar; a liquid accelerator is dosed at 4% by mass and a retarder at 130 mL per 100 kg of mortar. Bead dimensions were measured from deposited test filaments: the primary bead is 30 by 10 mm in cross-section (area 300 mm²) and the lamination bead is 20 by 8 mm (area 160 mm²). Fresh density is

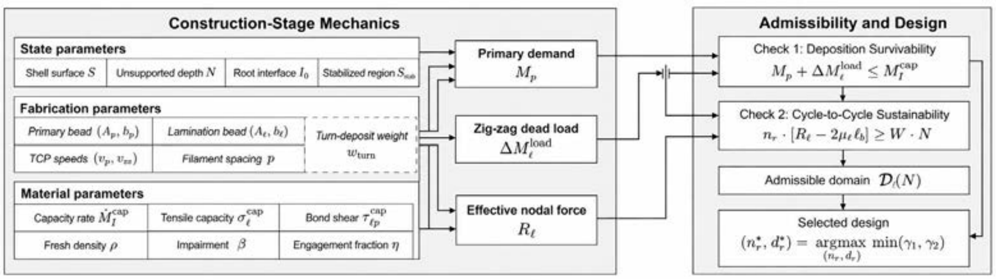

10

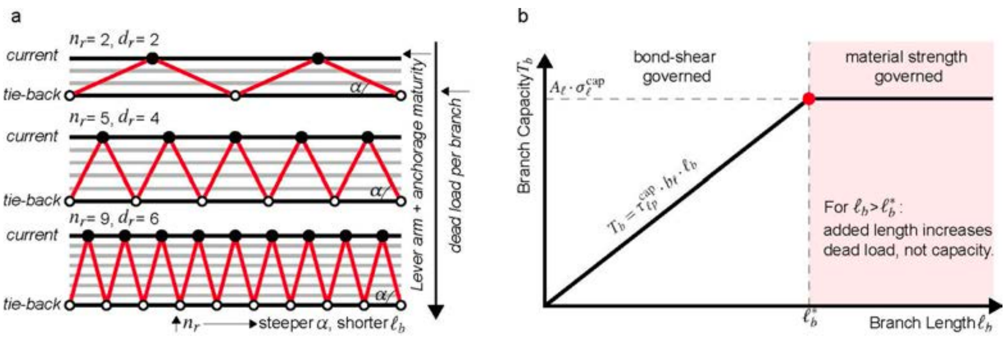

11

12

10 Reduced-order admissibility framework. Geometric, fabrication, and material inputs determine primary demand, pre-bond zig-zag dead load, and post-bond restoring force. Checks 1 and 2 define the admissible domain, and the max-min margin criterion selects an interior design.

11 Branch-mechanics trade-off: varying restraint-node count nr and tie-back depth d_r (a), and branch-capacity regimes separated by the crossover length ℓ_b^* (b).

12 Barrel-vault demonstrator fabrication setup: six-axis industrial robot on a linear rail, inline two-component mixing head at the end effector, and a custom steel support frame defining the springing/startup zone.

2100 kg/m³, measured from deposited samples. Filament tensile capacity and the interfacial bond shear strength were determined from early-age characterization tests on the same mix at ages representative of the construction window (1–3 minutes), giving an admissible axial stress of 40 kPa and a bond traction of 5 kPa. Primary filaments were deposited at 60 mm/s; the zig-zag pass at 50 mm/s to accommodate turn decelerations. No waiting period was introduced between primary and zig-zag deposition. The turn-deposit weight at each reversal, measured separately on flat-substrate deposition tests at the same process settings, is 0.66 N per reversal.

Primary-layer-only print and its simulation

The first experiment is the primary-layer-only print, with no zig-zag lamination, intended to expose where the construction-stage failure occurs in the absence of any tie-back action. The cantilevering portion failed at 42 millimeters beyond the initial root interface, corresponding to three unsupported filaments. The cantilever peeled away cleanly at the root interface, the interlayer boundary between the supported startup zone and the first unsupported primary filament.

We applied the FEM of Section 3.1 to the same geometry. The vault was discretized with 150 hexahedral elements along the span, fifteen layers along the print direction, and one element through the thickness. The intrados of the supported layers and the springing faces were clamped through Nitsche boundary conditions; all remaining surfaces were traction-free. The cohesive law was assigned fracture energies drawn from published ranges for cementitious interfaces (Keita et al. 2019). The simulation reproduces the experimentally observed progression through failure onset: the stable supported base, the onset of progressive downward deflection once the print extends beyond the supported region, and separation at the interface between supported and cantilevering regions (Figure 13). Throughout the simulated build, damage concentrates on a single interlayer facet at the boundary between supported and unsupported material; no other interlayer interface develops damage. The governing failure mechanism is therefore interlayer separation at one specific facet—the root of the cantilever— which is the localization that the reduced-order framework of Section 3.2 operationalizes.

Calibration of the Empirical Inputs

The framework requires three empirical inputs that cannot be determined from geometry or material tests alone: (a) the rate at which the root interface capacity grows during deposition, (b) the fraction of zig-zag deposition time credited toward capacity growth while the interface is already loaded (the capacity-impairment factor), and (c) the engagement fraction that scales the nominal post-bond branch capacity into the restoring force actually mobilized at each restraint node. We identify the three sequentially. The primary-layer-only print of Section 4.2 fixed the capacity rate from a single failure event: the elapsed time at failure together with the corresponding root moment yielded a capacity rate of 7.79×10^{-3} N·m·s^{-1} under the tested process conditions. The capacity-impairment factor was bounded using three configurations with different restraint-node counts and tie-back depths: C1 ($n_r = 10$, $d_r = 3$), C2 ($n_r = 12$, $d_r = 4$), and C3 ($n_r = 35$, $d_r = 2$) (Figure 14). All were deliberately driven to root-interface peel, the mode targeted by Check 1. For each failed design, equating demand and capacity gives the critical β at which it would become admissible; failure therefore places the true β below that value. The three experiments yield three upper bounds (Figure 15). The binding bound, $\beta = 0.30$ from C1, was adopted as the least conservative value consistent with all failures and correctly classifies C1–C3 as inadmissible. Because all calibration prints failed before Check 2 engaged, η remained a free parameter. The selected design was unchanged from one-third to full engagement.

Admissible domain and design selection

With tcapacity rate and β fixed, the two checks define the integer admissible domain (Figure 16). Check 1 is independent of η; Check 2 shifts with η but does not control selection over the tested range. Among admissible pairs, the max-min criterion in Figure 10 selects the design maximizing $\min(\gamma_1, \gamma_2)$, favoring balanced reserve rather than minimum material or time. The selected design $(n_r, d_r) = (7, 4)$, remains admissible for all η considered, with a $+22\%$ pre-bond margin. C1 and C2 lie outside the plotted Check 1 boundary; C3 $(35, 2)$ also fails Check 1 but lies beyond the plotted nr range.

Validation print

The validation used one primary and one zig-zag pass per cycle. The vault reached closure without delamination or visible distress, whereas the identical primary-only setup failed after three unsupported filaments (Figure 17). The result supports the selected design's admissibility and establishes $\eta \geq 0.32$ for the tested process; it does not independently verify the exact $+22\%$ analytical margin.

DISCUSSION

The admissible domain contains feasible but non-equivalent designs. Near Check 1, longer or denser laminations add pre-bond weight and deposition time; near Check 2, branch action provides little reserve. Designers may trade material and cycle time against robustness and surface articulation. Fewer nodes and shallower tie-backs reduce reversals, path length, and over-deposition; interior solutions tolerate more process variation. The max-min criterion selected $(7, 4)$ as a balanced interior solution, not a

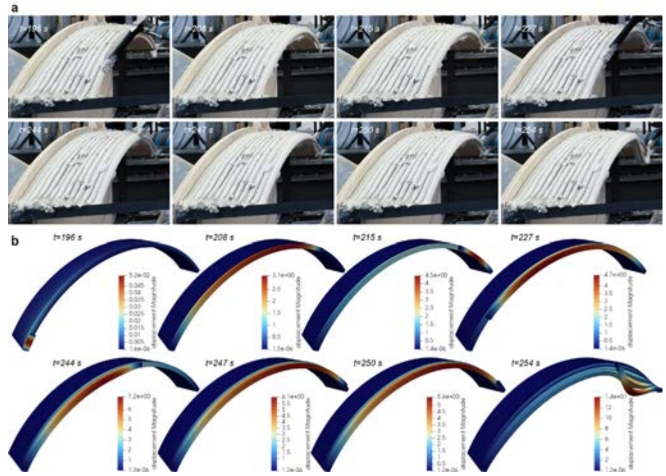

13

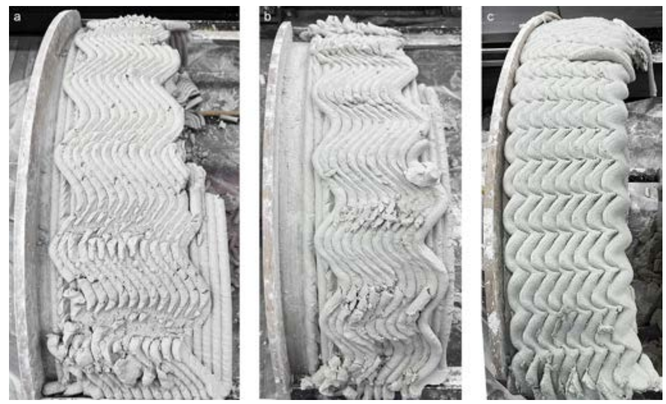

14

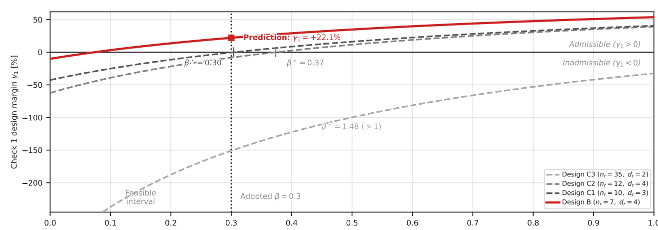

15

13 Primary-layer-only print and its simulation: experimental photographs at successive print stages (a) and simulated displacement magnitude at the same stages (b). Damage concentrates on a single interlayer facet at the boundary between supported and unsupported material.

14 Calibration configurations C1 ($n_r = 10$, $d_r = 3$), C2 ($n_r = 12$, $d_r = 4$), and C3 ($n_r = 35$, $d_r = 2$), deliberately driven to failure to bound the capacity-impairment factor. All three failed by peel at the root interface.

15 Identification of the capacity-impairment factor: Check 1 design margin plotted against the impairment factor for each design. The binding bound is 0.30 from design C1.

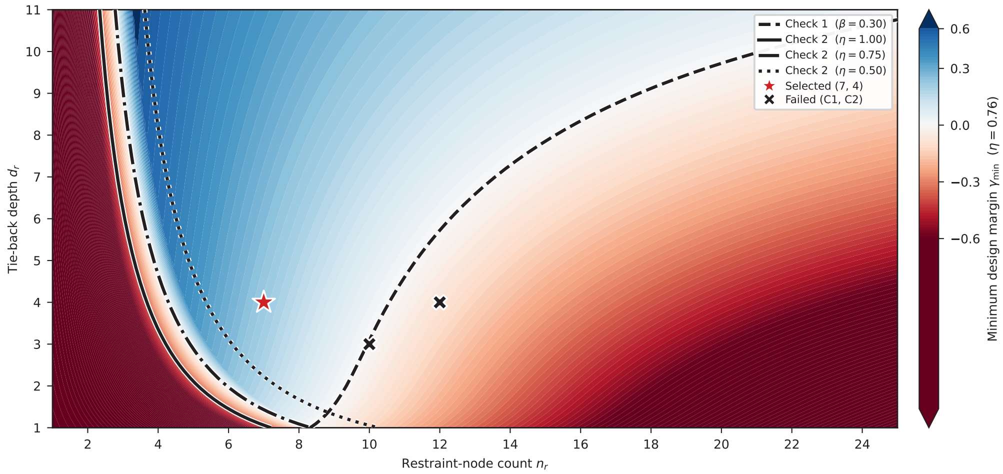

16

16 Admissible domain at three engagement fractions. The selected design is admissible; failed designs C1 and C2 are shown outside Check 1, while C3 lies beyond the plotted restraint-node range.

17 Successful validation print using the selected lamination design: top view of the deposited zig-zag lamination pattern across the completed vault.

universal optimum. The FEM and reduced-order model have distinct roles. The FEM diagnoses primary-only failure mode, location, and onset but does not simulate the zig-zag. The screening model assumes that root-interface peel remains the governing failure mode and represents bond activation through limiting pre- and post-bond states rather than continuous kinetics. Validation covers one barrel geometry, material system, and process window. Capacity rate came from one primary-only failure, β from three failed laminations, and η from one successful print. The results support the tested mechanism and classification; other materials, bead geometries, speeds, or double-curved shells require recalibration and renewed FEM diagnosis if the governing mode changes.

CONCLUSION

This paper presents a cohesive lamination method for scaffold-free robotic 3DCP of vaults that pass through cantilevering construction stages. A secondary zig-zag creates tension ties that anchor the active primary front into stabilized material, translating Guastavino's cross-bonded logic into continuous deposition. A cohesive-interface FEM identified root-interface delamination in the primary-only sequence; the reduced-order framework then screened combinations of restraint-node count and tie-back depth using deposition survivability and cycle-to-cycle sustainability. In In the demonstrator, which had a span of 1200 mm and a rise of 300 mm,, the primary-only sequence failed after three unsupported filaments, while the selected lamination completed the vault without internal scaffolding. Future work will extend the method to nonuniform and double-curved vaults, integrate the checks with adaptive robotic planning, and quantify how the construction-stage lamination contributes to the hardened vault's service-stage stiffness and capacity.

REFERENCES

Bhooshan, Shajay, Vishu Bhooshan, Johannes Megens, Tommaso Casucci, Tom Van Mele, and Philippe Block. 2022. "Print-Path Design for Inclined-Plane Robotic 3D Printing of Unreinforced Concrete." In Robotic Fabrication in Architecture, Art and Design 2022: Towards Radical Regeneration, 188–197. Cham: Springer International Publishing.

Block, Philippe. 2009. "Thrust Network Analysis: Exploring Three-Dimensional Equilibrium." PhD diss., Massachusetts Institute of Technology.

Borg Costanzi, Costanzo, Zeeshan Y. Ahmed, Hans R. Schipper, Freek P. Bos, Ulrich Knaack, and Rob J. M. Wolfs. 2018. "3D Printing Concrete on Temporary Surfaces: The Design and Fabrication of a Concrete Shell Structure." Automation in Construction 94: 395–404.

Brodmann, Anton, Efstathios Damtsas, Christoph Schult, Benjamin Spaeth, and Michael Herrmann. 2024. "DesignBuild Project of a 3D Printed Concrete Shell with a Segmented and Stereotomic Construction Concept." In Proceedings of the 42nd International Conference on Education and Research in Computer Aided Architectural Design in Europe (eCAADe), vol. 1, 105–114. Nicosia: eCAADe.

Buswell, Richard A., Wilson R. Leal de Silva, Scott Z. Jones, and Justin Dirrenberger. 2018. "3D Printing Using Concrete Extrusion: A Roadmap for Research." Cement and Concrete Research 112: 37–49.

Carneau, Paul, Romain Mesnil, Nicolas Roussel, and Olivier Baverel. 2019. "An Exploration of 3D Printing Design Space Inspired by Masonry." In Proceedings of the IASS Annual Symposium 2019: Structural Membranes 2019: Form and Force, 1–10. Barcelona.

Carneau, Paul, Romain Mesnil, Nicolas Roussel, and Olivier Baverel. 2020. "Additive Manufacturing of Cantilever: From Masonry to Concrete 3D Printing." Automation in Construction 116: 103184.

Collins, George R. 1968. "The Transfer of Thin Masonry Vaulting from Spain to America." Journal of the Society of Architectural Historians 27 (3): 176–201.

Dell'Endice, Andrea, Sara Bouten, Tom Van Mele, and Philippe Block. 2023. "Structural Design and Engineering of Striatus, an Unreinforced 3D-Concrete-Printed Masonry Arch Bridge." Engineering Structures 292: 116534.

Guastavino, Rafael. 1893. Essay on the Theory and History of Cohesive Construction, Applied Especially to the Timbrel Vault. Boston: Ticknor and Company.

Heyman, Jacques. 1966. "The Stone Skeleton." International Journal of Solids and Structures 2 (2): 249–279.

Jipa, Andrei, Ana Anton, Lukas Gebhard, and Benjamin Dillenburger. 2024. "The Nubian Slab: 3D Concrete Printed Stay-in-Place Formwork for Vaulted Slabs." In Fourth RILEM International Conference on Concrete and Digital Fabrication, 389–396. Cham: Springer Nature Switzerland.

Keita, Emmanuel, Hela Bessaies-Bey, Wenqiang Zuo, Patrick Belin, and Nicolas Roussel. 2019. "Weak Bond Strength between Successive Layers in Extrusion-Based Additive Manufacturing: Measurement and Physical Origin." Cement and Concrete Research 123:

17

105787.

Mechtcherine, Viktor, Freek P. Bos, Arnaud Perrot, Wilson R. Leal da Silva, Venkatesh N. Nerella, Shahin Fataei, Rob J. M. Wolfs, Mohammed Sonebi, and Nicolas Roussel. 2020. "Extrusion-Based Additive Manufacturing with Cement-Based Materials—Production Steps, Processes, and Their Underlying Physics: A Review." Cement and Concrete Research 132: 106037.

Meyer, Christian, and Michael H. Sheer. 2005. "Do Concrete Shells Deserve Another Look?" Concrete International 27 (10): 43–50.

Motamedi, Mohammad, Romain Mesnil, Robin Oval, and Olivier Baverel. 2022. "Scaffold-Free 3D Printing of Shells: Introduction to Patching Grammar." Automation in Construction 139: 104306.

Ochsendorf, John. 2010. Guastavino Vaulting: The Art of Structural Tile. New York: Princeton Architectural Press.

Roussel, Nicolas. 2006. "A Thixotropy Model for Fresh Fluid Concretes: Theory, Validation and Applications." Cement and Concrete Research 36 (10): 1797–1806.

Roussel, Nicolas. 2018. "Rheological Requirements for Printable Concretes." Cement and Concrete Research 112: 76–85.

Ruitinga, Volker, and Emma Chris Avramiea. 2024. "Custom-Made Printheads Empowering 3D Printed Concrete: Innovations in Digital Design and Fabrication of Complex Prefabricated Elements." In Coding Architecture, edited by Pierpaolo Ruttico, 239–261. Cham: Springer.

Sanjayan, Jay G., Behzad Nematollahi, Ming Xia, and Taylor Marchment. 2018. "Effect of Surface Moisture on Inter-Layer Strength of 3D Printed Concrete." Construction and Building Materials 172: 468–475.

Scheder-Bieschin, Lotte, Tom Van Mele, and Philippe Block. 2024. "Bending-Active Formwork Systems for Concrete Shells: A Classification and State-of-the-Art Review." Structures 67: 106841.

Suiker, Akke S. J. 2018. "Mechanical Performance of Wall Structures in 3D Printing Processes: Theory, Design Tools and Experiments." International Journal of Mechanical Sciences 137: 145–170.

Tang, Gabriel. 2015. "An Overview of Historical and Contemporary Concrete Shells, Their Construction and Factors in Their General Disappearance." International Journal of Space Structures 30 (1): 1–12.

Wangler, Timothy, Ena Lloret, Lex Reiter, Norman Hack, Fabio Gramazio, Matthias Kohler, Mathias Bernhard, Benjamin Dillenburger, Jonas Buchli, Nicolas Roussel, and Robert Flatt. 2016. "Digital Concrete: Opportunities and Challenges." RILEM Technical Letters 1: 67–75.

Wolfs, Rob J. M., Freek P. Bos, and Theo A. M. Salet. 2018. "Early Age Mechanical Behaviour of 3D Printed Concrete: Numerical Modelling and Experimental Testing." Cement and Concrete Research 106: 103–116.

IMAGE CREDITS

Figures 1, 2, 5–17: Images and drawings by the authors.
Figure 3: (a) Cámara, Proceso de construcción de las bóvedas, 1941; (b) Collins 1968; (c–d) Guastavino 1893.
Figure 4: Source images: (a) Dell'Endice et al. 2023; (b) Ruitinga and Avramiea 2024; (c) Jipa et al. 2024.

Abdallah Kamhawi is a Ph.D. researcher at the University of Michigan's Taubman College of Architecture and Urban Planning and the DART Laboratory. His research focuses on scaffold-free robotic 3D concrete printing, computational mechanics, materially informed print-path generation, and AI-enabled construction. .

Mania Aghaei Meibodi is an Assistant Professor of Architecture at the University of Michigan's and Director of the DART Laboratory. Her research integrates computational design, artificial intelligence, robotic fabrication, and construction-scale additive manufacturing to develop materially efficient building systems. She received the NSF CAREER Award in 2025 for her research on data-driven extrusion-based robotic 3D printing of reinforced concrete. She previously conducted research at ETH Zurich and holds a Ph.D. and professional degree in architecture from KTH Royal Institute of Technology.

Jesse Capecelatro is an Associate Professor of Mechanical Engineering and Aerospace Engineering at the University of Michigan and leads the Capecelatro Research Group. His research develops scalable numerical methods and data-driven models for complex multiphysics and multiphase flows, with applications in energy, the environment, and advanced manufacturing. He received his Ph.D. in Mechanical and Aerospace Engineering from Cornell University and is a recipient of the National Science Foundation CAREER Award and the Office of Naval Research Young Investigator Award.